Contents lists available at ScienceDirect

Brain Research

journal homepage: www.elsevier.com/locate/brainres

Susceptibility of neuroblastoma and glioblastoma cell lines to SARS-CoV-2 infection

Valéry Bielarz [a], Kévin Willemart [b], Noémie Avalosse [a], Kathleen De Swert [a], Riselane Lotfi [a], Noémie Lejeune [b], Florian Poulain [b], Noelle Ninanne [c], Jacques Gilloteaux [a,d], Nicolas Gillet [b], Charles Nicaise [a,*]

[a] URPhyM, NARILIS, Université de Namur, Namur, Belgium
[b] URVI, Université de Namur, Namur, Belgium
[c] URBC, Université de Namur, Namur, Belgium
[d] Department of Anatomical Sciences, St George's University School of Medicine, Newcastle upon Tyne, United Kingdom

ARTICLE INFO

ABSTRACT

Modelling cell infection in-a-dish can represent a useful tool to understand the susceptibility of different cell types towards severe acute respiratory coronavirus-2 (SARS-CoV-2) and to decipher its neurotropism. In this perspective, retinoic acid (RA)-differentiated neuroblastoma cell lines, SH-SY5Y and SK-N-BE(2) and glioblastoma cell lines, U-87 MG and U-373 MG, were infected with a SARS-CoV-2 strain, at various multiplicity-of-infection (MOI). We first demonstrated that the common entry genes – needed for invading epithelial cells – were expressed. RA-differentiation induced an upregulation of *ace2* and *tmprss2* gene expression while inducing downregulation of *ctsb* and *ctsl*. Using *in situ* hybridization and confocal analysis, SARS-CoV-2 *gene S* RNA was detected intracellularly at MOI 5.0, and localized in both soma and neuritic-like or glial-like processes. The infection was confirmed by quantification of viral *gene E* RNA and showed a dose-dependency, with few infected cells at MOI 0.1. After 24 h of infection, no cytopathic effect was observed in SH-SY5Y abilities to maintain neuritic processes or in U-373 MG for the uptake of glutamate. Unlike the permissive Vero E6 cells, no significant apoptosis death was detected following SARS-CoV-2 infection of neuroblastoma or glioblastoma cells. This study demonstrates the susceptibility of neuronal- and glial-like cell lines towards SARS-CoV-2 infection at high MOIs. Once inside the cells, the virus does not seem to rapidly replicate nor exert major cytopathic effect. Overall, our results strengthen the idea that SARS-CoV-2 has a tropism for nervous cells that express commonly described entry genes.

1. Introduction

Most of the time, the infection with severe acute respiratory syndrome coronavirus 2 (SARS-CoV-2) causes respiratory symptoms, known as coronavirus disease 2019 (COVID-19), although a minority of patients are at risk of developing a severe form with extrapulmonary involvements (for review (Gupta et al., 2020)). Severely SARS-CoV-2-affected patients are more likely to develop neurologic symptoms (e.g. headache, epilepsy, confusion, nausea and vomiting) than patients with a mild form of COVID-19 (Asadi-Pooya and Simani, 2020; Mao et al., 2020a; Paterson et al., 2020). Among the worst neurologic cases, viral encephalitis, necrotizing encephalopathy, acute myelitis or Guillain-Barré syndrome were reported (Chen et al., 2020; Kilinc et al., 2020; Mao et al., 2020a; Moriguchi et al., 2020; Poyiadji et al., 2020; Zhao

et al., 2020). Intriguingly, some patients developed neurologic symptoms even prior to any respiratory manifestation. In one retrospective study, up to 88% among the severe patients showed acute cerebrovascular diseases associated with impaired consciousness (Mao et al., 2020b). Neuro-imaging supports substantial brain damages in both COVID-19 survivors and non-survivors (Coolen et al., 2020; Helms et al., 2020; Zanin et al., 2020). Increasing evidences show the presence of SARS-Cov-2 in brain *post-mortem* tissue (Bulfamante et al., 2020; Paniz-Mondolfi et al., 2020; Puelles et al., 2020; Song et al., 2021), even though the mechanisms and routes of CNS entry are still elusive.

SARS-CoV-2 belongs to the same beta-coronaviruses family as SARS-CoV (2003 China outbreak) and shares up to 79,6% pairwise identities on a genomic level with its cousin (Lu et al., 2020). SARS-CoV-2 also shares common entry mechanisms used to invade target cells, including the binding of the spike (S) protein to human ACE2 receptor. S protein sequence was found to be approximately 77% homologous between SARS-CoV-2 and SARS-CoV. SARS-CoV-2 entry also depends on TMPRSS2 protease activity, which helps at ACE2 cleavage and receptor-binding domain unmasking, a condition required for membrane fusion (Hoffmann et al., 2020). Alternatively, cathepsin B or L may be able to substitute for TMPRSS2 in early endosomes upon endocytosis. ACE2 and TMPRSS2 have been detected at high expression levels in nasal, bronchial epithelium, as well as in alveolar epithelium (mostly type II pneumocytes), which explains the central respiratory pathology (Ortiz et al., 2020). Previously, neuro-invasion abilities of SARS-CoV have been firmly demonstrated on both patients and experimental animal models (Gu et al., 2005; Netland et al., 2008). Evidence from transgenic humanized ACE2 mice showed that SARS-CoV is able to enter the nervous system through the neuro-olfactory epithelium. It is then carried along the olfactory nerve up to the olfactory bulb, where it starts to spread to neighboring nervous cells (Netland et al., 2008). Similar SARS-CoV-2 neurotropic properties and CNS entry routes are under investigation. Of note, infected cells from the olfactory neuro-epithelium are suggested as gateways to central nervous system invasion in some individuals with COVID-19 (Cantuti-Castelvetri et al., 2020; Meinhardt

et al., 2020). Such an entry route was demonstrated as plausible in transgenic humanized ACE2 mice following experimental intranasal instillation of SARS-CoV-2 (Kumari et al., 2021).

So far, *in vitro* data showed the permissiveness of U-251 glioblastoma cell line to SARS-CoV-2 infection (Chu et al., 2020). Recently, evidences from five independent groups converge to show that human neural progenitor cells, grown either as neurospheres or as brain organoids, are susceptible to SARS-CoV-2 infection (Bullen et al., 2020; Ramani et al., 2020; Song et al., 2021; Yang et al., 2020; Zhang et al., 2020). In the present report, we aim at investigating the susceptibility of neuroblastoma and glioblastoma cell lines towards SARS-CoV-2 infection. These respective neuron-like and glial-like cells might represent useful tools to decipher the entry, replication and cytopathic effect of SARS-CoV-2 in the CNS.

2. Results

Before infecting the various neural cell lines with a Belgian SARS-CoV-2 strain, we sought to explore their expression level of entry genes, encoding proteins commonly needed by SARS-CoV-2 for invading human host cells. The transcripts for *ace2* and *tmprss2* genes were detected in both neuroblastoma (SH-SY5Y and SK-N-BE(2)) and both glioblastoma (U-87 MG and U-373 MG) cells, however in lower amounts than those of *hprt* housekeeping gene (Fig. 1a). Interestingly, RA-driven neuronal differentiation in SH-SY5Y and SK-N-BE(2) induced a significant upregulation of *ace2* mRNA, compared to undifferentiated cells ($0.0007197 \pm 7.698e\text{-}005$ *vs.* $0.003234 \pm 0,0005701$ in SH-SY5Y, $p < 0.05$; 0.004433 ± 0.00107 *vs.* 0.01072 ± 0.001291 in SK-N-BE(2), $p < 0.05$). Similarly, *tmprss2* gene expression was significantly induced upon RA differentiation ($0.0008177 \pm 6.422e\text{-}005$ *vs.* 0.005994 ± 0.0008207 in SH-SY5Y, $p < 0.05$; 0.05964 ± 0.02418 *vs.* 0.1956 ± 0.008158 in SK-N-BE(2), $p < 0.05$, RA-differentiated cells *vs.* undifferentiated cells). No comparison was made between cell lines due to variable amounts of *hprt* housekeeping gene. The transcripts of cathepsin B and L were expressed at higher levels than *hprt* across all cell lines analyzed (Fig. 1b). RA-
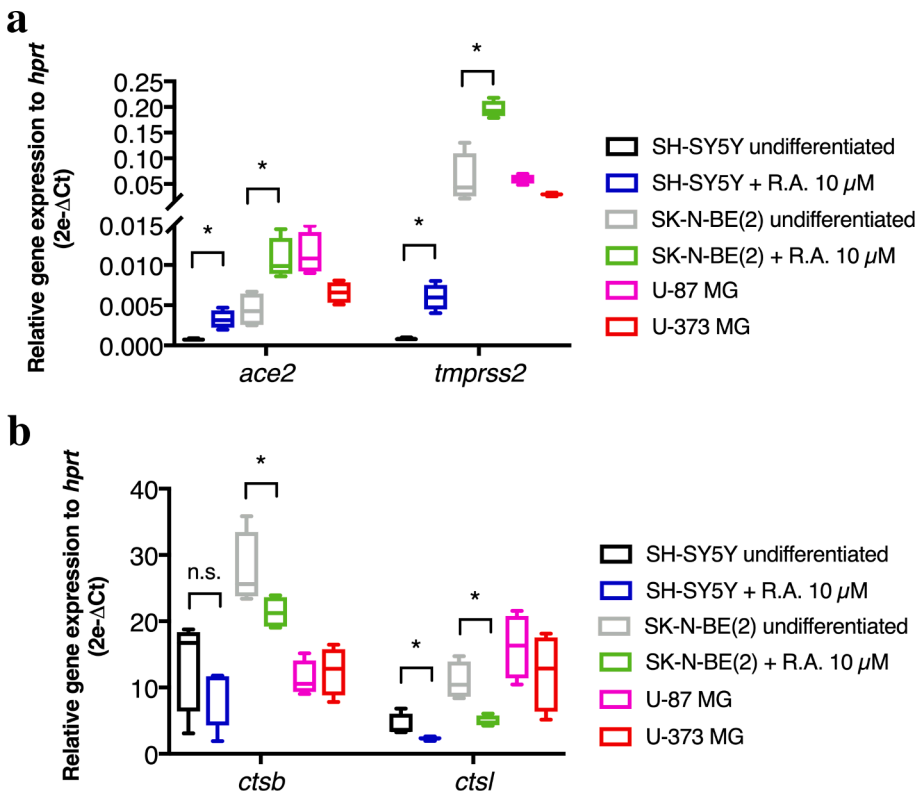
Fig. 1. Relative quantification of SARS-CoV-2 entry genes in human neural cell lines: *ace2* and *tmprss2* (a); *ctsb* and *ctsl* (b). Ct cycles for entry genes were normalized to Ct cycles of human *hprt* and relative expression data were expressed as 2e-ΔCt. Statistical significance was assessed using Mann-Whitney only on SH-SY5Y and SK-N-BE(2) cells with or without RA-based differentiation. *p < 0.05. Each box plots the median and extends from the 25th to 75th percentiles. Whiskers shows the min. and max. values. n = 4 independent samples per condition.

induced differentiation produced a significant downregulation of *ctsb* mRNA in SK-N-BE(2) cells (27.61 ± 2.809 *vs.* 21.35 ± 1.185, $p = 0.05$). Additionally, RA-induced differentiation produced a significant downregulation of *ctsl* mRNA in both SH-SY5Y and SK-N-BE(2) (4.317 ± 0.8435 *vs.* 2.311 ± 0.1334, $p < 0.05$; 10.99 ± 1.412 *vs.* 4.942 ± 0.4085, $p < 0.05$, RA-differentiated cells *vs.* undifferentiated cells).

RA-differentiated SH-SY5Y and SK-N-BE(2) were infected with SARS-CoV-2 at various MOIs during 2 or 24 h. Viral RNA was revealed using fluorescent or chromogenic *in situ* hybridization (*ish*) targeting the *gene S*. After 24 h at a MOI 5.0 of infection, *ish* signal was visualized in the cell bodies (black arrow), and to a certain extent in the neuritic processes (arrowheads in Fig. 2a). At MOI 0.1 and 1.0, *ish* signal was much sparser, probably reflecting a fewer number of infected neuroblastoma cells (data not shown). In comparison, infection of highly permissive VeroE6 cells with a MOI of 0.1 during 24 h produces a massive *ish* signal in the cytoplasmic compartment (Fig. 2a). The entry of viral particles in neuroblastoma cell lines was quantified using a qRT-PCR targeting the SARS-CoV-2 *gene E* (Fig. 2b). In SH-SY5Y, a 24 h infection with MOIs 1.0 and 5.0 produced a significant amplification of SARS-CoV-2 RNA from lyzed cells, in a dose-dependent manner (respectively 1.398 ± 0.0976, $p < 0.05$; 10.73 ± 0.7595, $p < 0.001$ when compared to mock condition). Noteworthy, the relative amount of *gene E* detected was higher when SH-SY5Y cells were infected at MOI 5.0 for 24 h than for 2 h (10.73 ± 0.7595 *vs.* 5.713 ± 0.1542, $p < 0.001$). In SK-N-BE(2) cells, only the highest MOI produced a significant infection at both timings, when compared to mock condition (respectively 1.443 ± 0.4262, $p < 0.001$ and 1.284 ± 0.09506, $p < 0.001$). No difference of viral RNA amount was observed between 2 h and 24 h of infection. Given that neither transmitted light microscopy or qRT-PCR assays could provide a definitive answer about the viral entry – i.e. viral particles could be adsorbed at the cell surface non-specifically or receptor-bound – into host cells, we assessed the intracellular localization of viral RNA by confocal analysis. The cytoskeleton of SH-SY5Y and SK-N-BE(2) cells was visualized using immunofluorescence against α-tubulin while SARS-CoV-2 gene S was revealed using fluorescent *ish* (Fig. 2c). In both cell lines, viral RNA was found in the same confocal plane as α-tubulin network. Further analysis of fluorescence intensity confirmed that fluorescent peaks, corresponding to SARS-CoV-2 gene S (red) and to α-tubulin (green), were overlapping (asterix in Suppl. Fig. 1).

We next investigated a cytopathic effect of SARS-CoV-2 once inside the cells by measuring the length of neuritic processes grown by RA-differentiated SH-SY5Y (Fig. 2d). No effect of SARS-CoV-2 infection was observed on the abilities of differentiated SH-SY5Y cells to maintain their neurites, even at the highest MOI of 5.0 after 24 h of infection (52.72 ± 2.167 μm compared to 52.98 ± 2.037 μm in mock condition, $p =$ n.s.). In the same line, we sought to know whether SARS-CoV-2 could induce cell death in infected nervous cell lines. The apoptosis rate was quantified in VeroE6 cells and compared to infected SH-SY5Y and SK-N-BE(2) cells (Fig. 2e). While VeroE6 cells are highly permissive to SARS-CoV-2 (Fig. 2a) and are therefore used to amplify the virus, many of infected cells undergo apoptosis-mediated cell death upon replication and/or release of viral particles. In VeroE6, the number of cleaved caspase-3 immunoreactive cells reached up to $25.33 \pm 2.603\%$ upon exposure to MOI 5.0 during 24 h, compared to $2.000 \pm 0.5774\%$ in mock condition ($p < 0.001$). Interestingly, neither SH-SY5Y or SK-N-BE(2) showed overt apoptosis upon infection with SARS-CoV-2, at any MOIs tested. For instance, the percentages of apoptotic cells were respectively $3.66 \pm 2.66\%$ and $7.00 \pm 4.04\%$ at MOI 5.0 in SH-SY5Y and SK-N-BE(2) ($p =$ n.s., compared to $2.50 \pm 0.88\%$ in mock conditions). Overall, both neuroblastoma cell lines were much less prone to apoptosis than VeroE6 cells at comparable MOIs (two-way ANOVA, VeroE6 *vs.* SH-SY5Y: $F_{(1,16)} = 44.21$, $p < 0.001$; VeroE6 *vs.* SK-N-BE(2) : $F_{(1,16)} = 30.61$, $p < 0.001$).

In order to evaluate the susceptibility of neural cell lines closer to a glial phenotype, U-87 MG and U-373 MG glioblastoma cell lines were infected with SARS-CoV-2 according to the same paradigm as neuroblastoma cells. At 2- or 24-hours post-infection, viral RNA was revealed

using chromogenic *in situ* hybridization targeting the *gene S* (Fig. 3a). Following 24 h at MOI 5.0, infected cells showed obvious *ish* chromogenic deposits in the cell bodies as well as in the glial-like processes (inset in Fig. 2a). The entry of viral particles in glioblastoma cells was also quantified using qRT-PCR (Fig. 3b). In U-87 MG cells, a 24-hour infection produced a significant amplification of SARS-CoV-2 RNA, in a dose-dependent manner (0.323 ± 0.05743 for MOI 1.0, $p < 0.01$ and 1.125 ± 0.07618 for MOI 5.0, $p < 0.001$ compared to mock condition). Even though the levels of infection followed a similar profile at 2 h post-infection, the relative amount of SARS-CoV-2 *gene E* was significantly lower at 24 h than at 2 h of infection for MOI 5.0 (1.125 ± 0.07618 *vs.* 1.617 ± 0.1079, $p < 0.001$). In U-373 MG, only the highest MOI at 2 h of infection led to a significant detection of viral RNA, compared to mock condition (2.117 ± 0.2568 *vs.* 0.0 ± 0.0 undetected, $p < 0.001$) (Fig. 3b). A 24-hour infection produced a significant amplification in a dose-dependent manner (0.9433 ± 0.0382 for MOI 1.0, $p < 0.01$ and 3.671 ± 0.4731 for MOI 5.0, $p < 0.001$ compared to mock condition). At MOI 5.0, a longer infection time led to increased amount of *gene E* detected in U-373 MG (2.117 ± 0.2568 at 2 h *vs.* 3.671 ± 0.4731 at 24 h, $p < 0.001$).

U-87 and U-373 cell lines are both considered as glioblastoma cells comprising a heterogeneous mixture of morphologically, biochemically and functionally distinct cancer cells. For instance, they are both classified as astrocytoma cells but differ in terms of GFAP expression. Grown on uncoated plastic culture dishes, U-87 MG cells are GFAP^{low} expressing cells whereas U-373 MG cells are GFAP[high]-expressing cells (Fig. 3c). Both cell lines, no matter they express low or high GFAP levels, are susceptible to SARS-CoV-2 infection. U-87 and U-373 also differ in glutamate uptake abilities, even though all glioma cell lines showed impaired glutamate uptake compared to normal human astrocytes (Ye and Sontheimer, 1999). While U-87 cells have lost this ability (data not shown), U-373 MG cells internalized glutamate upon addition of 200 μM of glutamate in the medium (111.4 ± 3.452 μM compared to 224.7 ± 8.722 μM in basal medium without cells, $p < 0.001$) (Fig. 3d). Infection with various MOIs of SARS-CoV-2 during 24 h did not impact U-373 cells in their glutamate uptake abilities (one-way ANOVA, $p = 0.4668$ mock *vs.* MOI 0.1; $p = 0.0955$ mock *vs.* MOI 1.0; $p = 0.9664$ mock *vs.* MOI 5.0). Finally, SARS-CoV-2 cytopathic effect on glioblastoma cells was evaluated by counting the number of cleaved caspase-3 positive cells at 24 h of infection (Fig. 3e). Infected U-87 or U-373 did not show more apoptosis at any MOI tested than mock condition. For instance, the percentages of apoptotic cells were respectively $5.00 \pm 3.60\%$ and $8.33 \pm 0.88\%$ at MOI 5.0 in U-87 and U-373 ($p =$ n.s., compared to $2.83 \pm 0.83\%$ in mock conditions). Overall, glioblastoma cell lines were much less prone to apoptotic cell death than VeroE6 cells at comparable MOIs (two-way ANOVA, VeroE6 *vs.* U-87 MG: $F_{(1,16)} = 38.70$, $p < 0.001$; VeroE6 *vs.* U-373 MG : $F_{(1,16)} = 38.78$, $p < 0.001$).

3. Discussion

Our main findings are that SARS-CoV-2 is able to invade neuroblastoma and glioblastoma cell lines, without exerting major cytopathic effect on either neuron-like morphology or on functional glutamate uptake, and without inducing obvious apoptosis. Although the viral entry-dependency on common entry genes was not investigated, a basal expression of ace2, tmprss2, cathepsin B and cathepsin L transcripts was detected in all cell lines. Noteworthy, RA-differentiated neuroblastoma cells upregulated the gene expression of surface receptors such as ace2 and tmprss2. The definitive entry mechanisms inside nervous cells are still debated and existence of alternative surface receptors that might be hijacked cannot be ruled out, as it is described for SARS-CoV and some epithelial cells or immune cells e.g. CD147/BSG, CD26/DPP4 (Radzikowska et al., 2020).

Our experimental design allows to conclude that neuroblastoma and glioblastoma cells are modestly susceptible to SARS-CoV-2 infection, based on the high MOI needed to infect cells. In comparison to recent
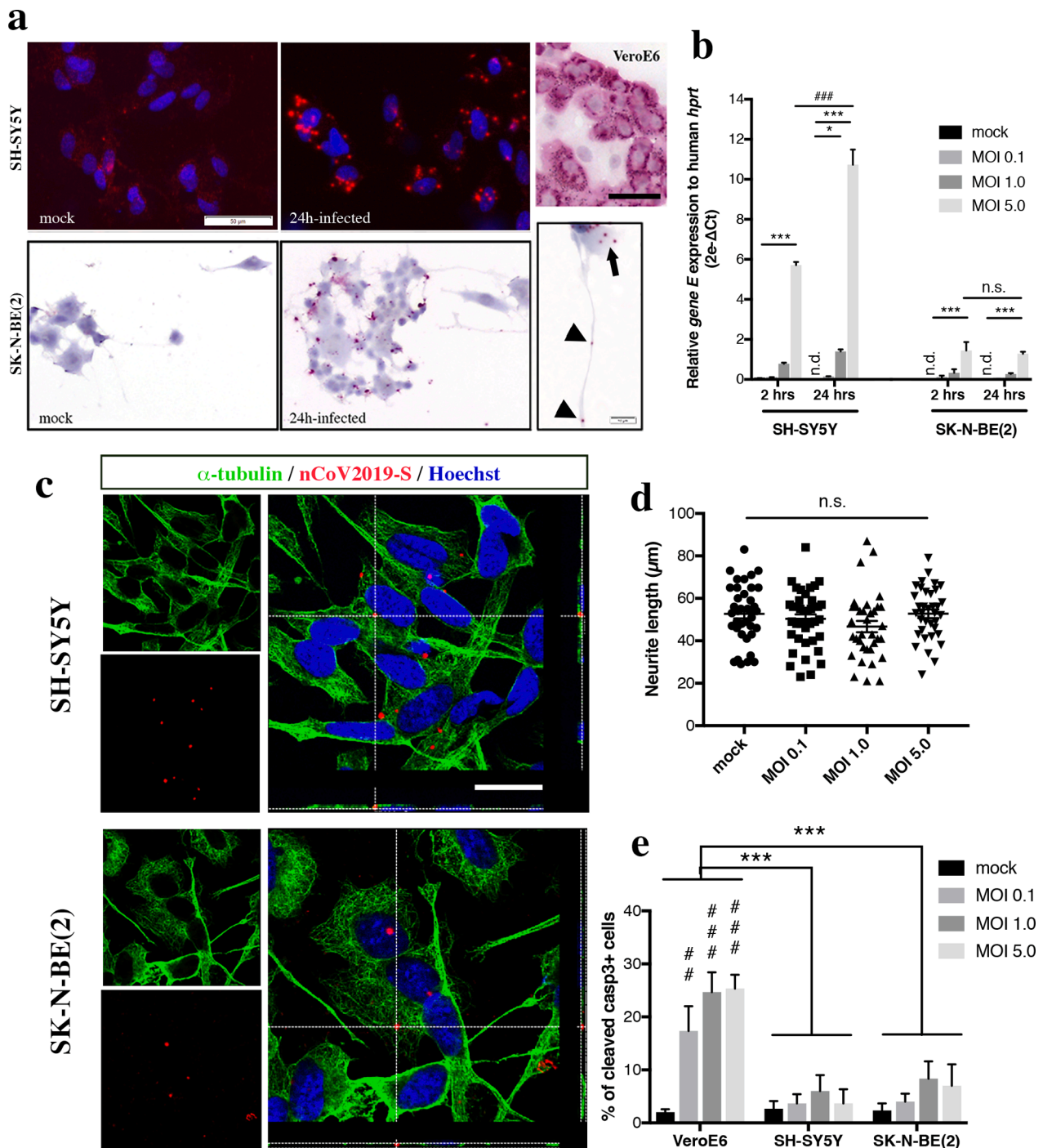
Fig. 2. Chromogenic or fluorescent *in situ* hybridization (*ish*) using SARS-CoV-2 *gene S* probe (nCoV2019-S, red) were applied on RA-differentiated SH-SY5Y and SK-N-BE(2) cells exposed to SARS-CoV-2 at MOI 5.0 during 24 h or to mock condition (a). Nuclei were counterstained with Hoechst (blue). Scale bar represents 50 μm. Viral RNA was detected in the cell body compartment of infected cells (black arrow) as well as along the neuritic processes (black arrowheads). Scale bar represents 10 μm. In comparison, infection of epithelial VeroE6 cells with a lower MOI (0.1) of SARS-CoV-2 produced a massive *ish* signal in the cytoplasmic compartment (upper right panel). Scale bar represents 20 μm. Quantification of SARS-CoV-2 *gene E* relative abundance in infected SH-SY5Y and SK-N-BE(2) according to various MOIs and timings of infection (b). Ct cycles for *gene E* were normalized to Ct cycles of human *hprt* and relative expression data were expressed as 2e-ΔCt. Statistical significance was calculated using a two-way ANOVA comparing each MOI and each timing. *$p < 0.05$; ***$p < 0.001$ for comparisons between each MOI, ###$p < 0.001$ for comparisons between 2 h and 24 h of infection. n = 3 independent samples for each condition. Representative multiplex nCoV2019S *ish* (red)/ α-tubulin (green) immunofluorescence images showed that viral RNA was in the same confocal plane as the cytoskeleton network in both infected neuroblastoma cell lines, when cells were infected at MOI 5.0 during 24 h (c). Scale bar represents 25 μm. Orthogonal views from z-stack reconstruction confirmed the intracellular localization of SARS-CoV-2 RNA signal. At 24 h of infection, SARS-CoV-2 cytopathic effect was assessed by measuring the length of neuritic processes grown by RA-differentiated SH-SY5Y cells (d). Statistical significance was calculated using a one-way ANOVA comparing each MOI to mock condition. N = 35–39 neurites counted per condition. At 24 h of infection, SARS-CoV-2 cytopathic effect was assessed by counting the number of cleaved caspase-3 immunoreactive SH-SY5Y or SK-N-BE(2) cells, and compared to MOI-matched VeroE6 cells (e). Statistical significance was calculated using a two-way ANOVA comparing each MOI and each cell type. ***$p < 0.001$ for comparisons between VeroE6 and SH-SY5Y or SK-N-BE(2), ##$p < 0.01$, ###$p < 0.001$ for comparisons between MOI. N = 100 cell nuclei counted per condition. Abbreviations: MOI, multiplicity-of-infection; n.d., not detected; n.s., not significant.
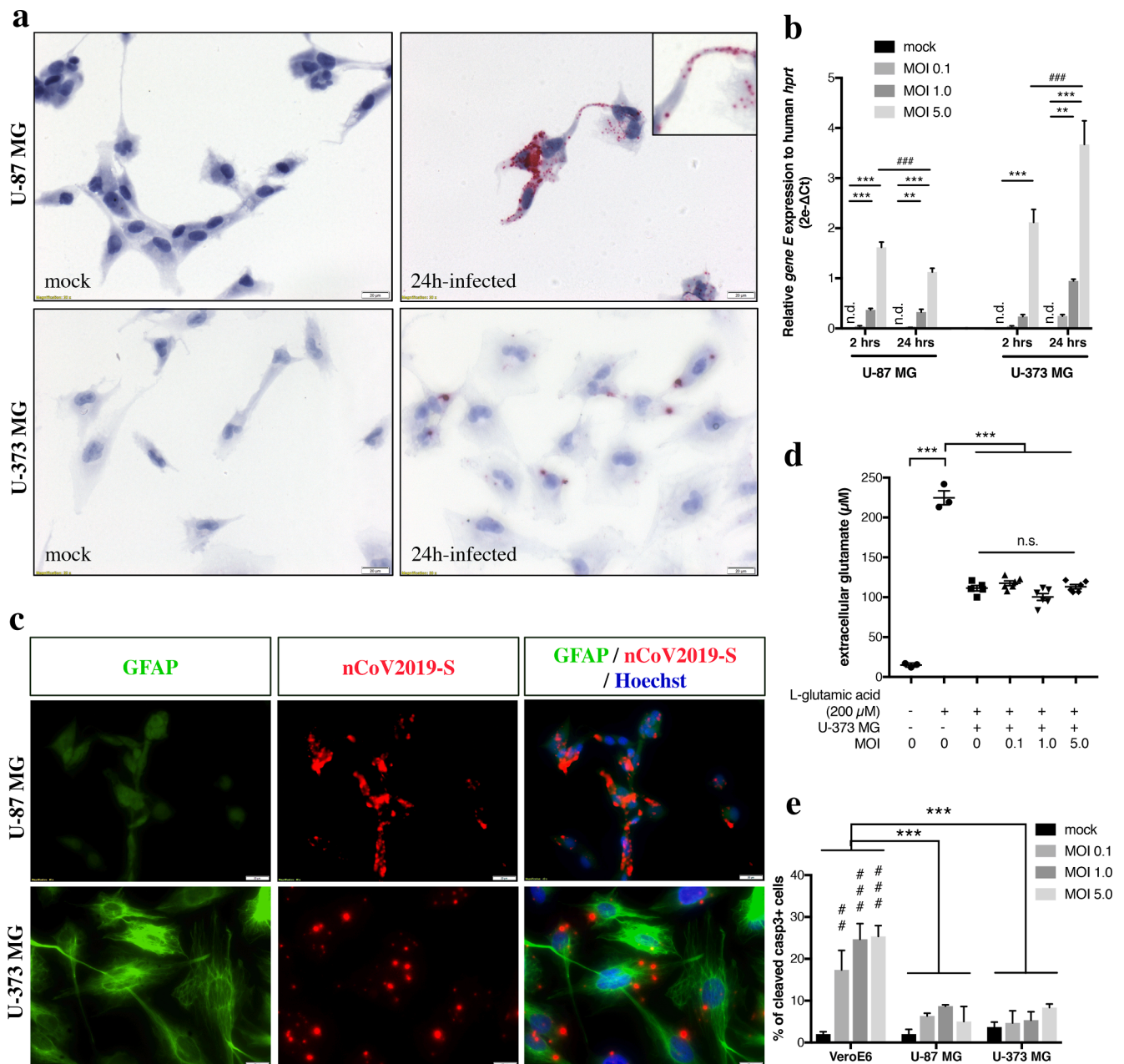
Fig. 3. Chromogenic *in situ* hybridization (*ish*) using SARS-CoV-2 *gene S* probe (nCoV2019-S) was applied on U-87 MG and U-373 MG cells exposed to SARS-CoV-2 at MOI 5.0 during 24 h or to mock condition (a). Scale bar represents 20 μm. Viral RNA was detected in the cell body compartment of infected cells as well as in the glial-like processes (inset in the upper right panel). Quantification of SARS-CoV-2 *gene E* relative abundance in infected SH-SY5Y and SK-N-BE(2) according to various MOIs and timings of infection (b). Ct cycles for *gene E* were normalized to Ct cycles of human *hprt* and relative expression data were expressed as 2e-ΔCt. Statistical significance was calculated using a two-way ANOVA comparing each MOI and each timing. **p < 0.01; ***p < 0.001 for comparisons between each MOI, ###p < 0.001 for comparisons between 2 h and 24 h of infection. N = 3 independent samples for each condition. Representative multiplex nCoV2019S *ish* (red)/ GFAP (green) immunofluorescence images showed SARS-CoV-2 abilities to infect both GFAP^{low}-expressing cells (U-87 MG) and GFAP^{high}-expressing cells (U-373 MG), upon infection with MOI 5.0 during 24 h (c). Scale bar represents 20 μm. At 24 h of infection, SARS-CoV-2 cytopathic effect was assessed by quantifying the ability of U-373 MG cells to take up extracellular glutamate added to the culture supernatant (200 μM) (d). Infected U-373 MG cells were able to pump up glutamate from supernatant as efficiently as non-infected cells (p = n.s.). Statistical significance was calculated using a one-way ANOVA comparing each MOI to mock condition. N = 6 independent samples per condition. At 24 h of infection, SARS-CoV-2 cytopathic effect was assessed by counting the number of cleaved caspase-3 immunoreactive U-87 MG or U-373 MG cells, and compared to MOI-matched VeroE6 cells (e). Statistical significance was calculated using a two-way ANOVA comparing each MOI and each cell type. ***p < 0.001 for comparisons between VeroE6 and U-87 MG or U-373 MG, ##p < 0.01, ###p < 0.001 for comparisons between MOI. n = 100 cell nuclei counted per condition. Abbreviations: MOI, multiplicity-of-infection; n.d., not detected; n.s., not significant.

studies, human brain organoids and neurospheres were respectively infected with MOIs of 10.0 and 0.1 (Bullen et al., 2020; Zhang et al., 2020). At early infection timings (24 h), neuroblastoma and glioblastoma cells were not as permissive as VeroE6 epithelial cells. So far, contradictory results are reported about the SARS-CoV-2 replication into

human neurons. While one study showed that SARS-CoV-2 entered neurons from brain organoids but did not replicate (Ramani et al., 2020), in two studies genomic viral material was found in the supernatant at higher level several hours post-infection than at the time zero of infection, which supports the release of new viral particles (Bullen

et al., 2020; Zhang et al., 2020). Intriguingly, we did not observe major SARS-CoV-2 cytopathic effect on any cell lines, unlike what was described in infected brain neurospheres or despite the evidences of neuronal and astrocytic injury in COVID-19 patients (Kanberg et al., 2020; Ramani et al., 2020). This might be explained by a better resistance of tumor cell lines towards SARS-CoV-2 infection or a too short timing for apoptosis analysis.

Bearing in mind the limitation that *in situ* hybridization – and not immunofluorescence nor electron microscopy – was used throughout this study to detect SARS-CoV-2, our confocal images comforted the intracellular localization of viral RNA. Interestingly, viral RNA was distributed in both soma, and neuron-like or glial-like extensions. So far, we did not investigate whether this distribution was due to random internalization along the cell membrane or whether internalized viral particles were able to be transported inside/along the cell processes. This last concept is relevant for deciphering the CNS entry routes. Among the entry pathways, the retrograde transport along nerve fibers from peripheral infected tissues (i.e. nasal cavity) or the hematogenous pathway across the blood–brain barrier (BBB) are being demonstrated (Meinhardt et al., 2020; Uversky et al., 2020). From our images showing SARS-CoV-2 RNA in the cell processes, it is tempting to hypothesize that neuron-like or glial-like cells might internalize viral particles at their farthest cell extension and then, using intracellular trafficking, carry them back to the soma. Corollary, SARS-CoV-2 might penetrate the CNS gate by first invading brain endothelial cells or following BBB disruption, then being caught at the perivascular astrocytic processes (Uversky et al., 2020). This hypothesis is supported by ultrastructural findings from autopsied COVID-19 patients, where authors captured viral particles at the endothelial-astrocyte interface (Bulfamante et al., 2020; Paniz-Mondolfi et al., 2020). This passage would even be eased in the context of an important systemic inflammation that includes cytokines known to compromise BBB integrity (Uversky et al., 2020).

This study on SARS-CoV-2 cell tropism is complementary to those using human pluripotent stem cell-based platform (Yang et al., 2020). Infection of neuroblastoma or glioblastoma cells might serve as an easy and low-cost model for testing drugs that interfere with viral entry, e.g. ACE2 neutralizing antibodies, or other viral life cycle targets.

4. Experimental procedure

4.1. Cell culture

The SH-SY5Y neuroblastoma cell line, U-87 MG and U-373 MG glioblastoma cell lines were kindly provided by Profs. Jean-Pierre Brion and Karelle Leroy (Université Libre de Bruxelles, BE). The SK-N-BE(2) neuroblastoma cell line was a kind gift from Prof. Marielle Boonen (Université de Namur, BE). All cell lines were used between passage 15 and 25. They were maintained in DMEM/F12 (Life Technologies, Grand Island, NY, USA) supplemented with 10% fetal bovine serum (Sigma-Aldrich, Overijse, BE) and penicillin/streptomycin (Sigma-Aldrich, Overijse, BE / Millipore, USA). Cells were grown in a sterile incubator at 37 °C, 95% air humidity and 5% CO2 concentration. Culture medium was changed twice a week, depending on cell density, and cells were passaged for further cultivation or differentiation experiment at 80–90% confluency. For passaging, cells were trypsinized using 0.05% Trypsin/EDTA during 2 min, washed in medium and spun down at 130 g for 7 min and further split at a ratio 1:10. For differentiation experiment, SH-SY5Y and SK-N-BE(2) cells were seeded at a density of 20,000 cells per cm2, on glass coverslips pre-coated with 0.1 mg/ml Poly-L-lysine (Sigma-Aldrich, Overijse, BE). A differentiation protocol was applied based on 7 day-exposure to 10 μM all-trans-retinoic acid (RA) (Sigma-Aldrich, Overijse, BE) added in low-serum medium (DMEM/F12 + 2% FBS + penicillin/streptomycin). RA-driven differentiation was initiated 24 h after seeding and fresh medium was replaced everyday up to day 7. Vero cells, clone E6 (VeroE6), were used to amplify a purified SARS-CoV-2 strain isolated from a Belgian COVID-19 patient.

4.2. Infection with SARS-CoV-2

All infections or viral amplification were performed in a biosafety level-3 laboratory (Université de Namur, BE). The SARS-CoV-2 isolate was kindly provided by Prof. Piet Maes (KULeuven, BE). The viral titer of SARS-CoV-2 strain was determined by TCID50 on culture supernatant from infected Vero E6 cells. Neuroblastoma or glioblastoma cells were plated at a density of 20,000 cells per cm2 in a 24-well plate for *in situ* hybridization or a 12-well plate for gene expression studies. Cells were infected during 2- or 24-hours using a multiplicity-of-infection (MOI) of 0.1, 1.0 or 5.0 in low-serum medium. For mock condition, cells were incubated with the low-serum medium-only. At the end of infection, culture medium was carefully discarded. Cells were thoroughly washed three times with PBS and either lyzed in TriZol or chemically-fixed with 4% paraformaldehyde, ensuring virus inactivation.

4.3. RNA isolation and qRT-PCR

Cells were homogenized in 1 mL of Trizol reagent and total RNA was further isolated according to manufacturer's instructions (Life Technologies, Bleiswijk, NL). RNA concentrations were measured using a spetrophotometer Nanodrop 1000 (Thermo Scientific, Bleiswijk, NL). Total RNAs (1 μg), including viral and human RNAs, were reverse-transcribed using the Super Script II RNase H reverse transcriptase kit according to manufacturer's instructions (Invitrogen, Merelbeke, BE). cDNA was used to amplify SARS-CoV-2 *gene E* with Takyon Taqman kit and human genes with Takyon SYBR Green kit (Eurogentec, Liège, BE) in a Light Cycler 96 device (Roche Diagnostics, Mannheim, DE) (Coupeau et al., 2020). Primer sequences are listed in Table 1. Relative gene expression was computed using the ΔCq method with *hprt* as housekeeping gene.

4.4. In situ hybridization and immunofluorescence

Coverslips were fixed in cold 4% paraformaldehyde during 20 min and then washed and stored in PBS at 4 °C. Fixed cells were used within one-week post-fixation. Expression of SARS-CoV-2 *gene S* was detected according to manufacturer's kit instructions (RNAScope, Advanced Cell Diagnostics, Bio-techne, Abingdon, UK) and by using a specific target probe (RNAscope Probe-V-nCoV2019-S, #848561, Bio-techne, Abingdon, UK). Briefly, cells were permeabilized with PBS plus 0.1% Tween 20 for 10 min. After washing, endogenous peroxidases were blocked with hydrogen peroxide for 10 min followed by 2 washes in PBS. Cells were then incubated with RNAScope® Protease III (Advanced Cell Diagnostics Inc, Hayward, USA) for 10 min. and subsequently washed in PBS. Samples were incubated with the probe specifically targeting SARS-

Table 1
Primer and probe sequences for qRT-PCR.

Gene name (accession number)	Primer sense 5′-3′ Primer antisense 5′-3′ [Taqman probe]	Product length (bp)
human *ace2* (NM_001371415.1)	5′-GGACCCAGGAAATGTTCAGA-3′ 5′-GGCTGCAGAAAGTGACATGA-3′	238
human *tmprss2* (NM_001135099.1)	5′-CTGCCAAGGTGCTTCTCATT-3′ 5′-CTGTCACCCTGGCAAGAATC-3′	127
human *ctsb* (NM_147783)	5′-AGAGTTATGTTTACCGAGGACCT-3′ 5′-GATGCAGATCCGGTCAGAGA-3′	159
human *ctsl* (NM_145918)	5′-AAACTGGGAGGCTTATCTCACT-3′ 5′-GCATAATCCATTAGGCCACCAT-3′	97
human *hprt* (NM_000194.3)	5′-TGACACTGGCAAAACAATGCA-3′ 5′-GGTCCTTTTCACCAGCAAGCT-3′	94
SARS-CoV-2 *gene E* (NC_045512)	5′-ACAGGTACGTTAATAGTTAATAGCGT-3′ 5′-ATATTGCAGCAGTACGCACACA-3′ [(FAM)-ACACTAGCCATCCTTACTGCGCTTCG-(BHQ1)]	113

CoV-2 *gene S* mRNA (RNAScope, #422511, Advanced Cell Diagnostics, Bio-techne, Abingdon, UK) for 2 h at 40 °C and then washed for 2 min in RNAScope® wash buffer (Advanced Cell Diagnostics, Bio-techne, Abingdon, UK). Amplification rounds 1–6 alternated from 30 to 15 min at 40 °C. Between each amplification round, samples were washed with RNAScope® wash buffer. Detection of probe signals was performed by incubating samples with alkaline phosphatase (solution of RNA-Scope® Fast B and A ratio 1:60) for 10 min. at room temperature. Samples were then washed in milliQ water. Following *ish*, samples were either counterstained with hematoxylin (Sigma-Aldrich, Overijse, BE), dried for 30 min. at 60 °C and mounted using VectaMount® (Vector Laboratories, Burlingame, USA) or fluorescently stained according to the protocol below.

For *ish*/immunofluorescence multiplexing, coverslips were further washed 5 min at RT in PBS. Non-specific binding was blocked in a PBS-BSA 1% for 30 min at RT. Then, samples were incubated with primary antibodies in PBS-BSA 1% buffer overnight at RT: α-tubulin (1:500, T-5168, Sigma-Aldrich); GFAP (1:1000, G-3893, Sigma-Aldrich); cleaved caspase-3 (1:1000, #9664, Cell Signaling). After that, samples were washed 3X5 min with PBS-BSA 1%. Fluorophore-coupled secondary antibodies alexa fluor® 488 goat anti-mouse IgG 1:200 (#A11001, Life Technologies, Oregon, USA) or goat anti-rabbit IgG 1:200 (#A11008, Life Technologies, Oregon, USA) in PBS-BSA1% were applied on their respective tissue sections and incubated for 30 min at RT. Afterwards, they were washed 3X5 min with PBS-BSA 1% and cell nuclei were stained in a solution of Hoechst 33258 (Life Technologies, Oregon, USA). Finally, after 1×5 min wash with PBS-BSA 1% and 2X5 min with PBS, tissue sections were coverslipped with Mowiol mounting medium. Coverslips were imaged using an Olympus BX63 epifluorescence microscope equipped with SC50 camera for brightfield and XM10 camera for fluorescence.

4.5. Image analysis

Intracellular virus distribution was analyzed using a Leica TCS SP5 confocal microscope. Individual cells among those that were in focal field were randomly chosen and the spatial relationship between SARS-CoV-2 *ish* probe signal and cytoskeleton network (α-tubulin) was visually assessed. For each condition, 20 infected cells were at least acquired. All of the images were recorded at the same laser and multiplier settings.

For neurite length assessment, multiple representative brightfields of SH-SY5Y cells were imaged using an inverted microscope Olympus CKX41 equipped with EP50 camera. The channels were extracted to grey scale and the length of 5 to 10 neurites per field was traced and measured, thereafter, from the distal end of neuron growth-cone, using the neurite tracer plugin NeuronJ (ImageJ add-on software), according to published protocol (Pemberton et al., 2018). From the images, at least 35 neurites per condition were quantified.

For the analysis of caspase-3 immunolabeling, 100 cells per experimental condition were randomly acquired based on Hoescht nuclei counterstaining. The number of immunoreactive cleaved caspase-3+ cells was manually and blinded counted, and further related to 100 cell nuclei.

4.6. Glutamate uptake assay

The assay was adapted from Mahmoud et al. (Mahmoud et al., 2019). Briefly, 100,000 cells were seeded in each well of a 96-well plate, and washed 2 times with Hank's Balanced Salt Solution (HBSS) containing $Ca2+$ and $Mg2+$: 1.26 mM $CaCl2$, 5.36 mM KCl, 0.44 mM $KH2PO4$, 0.811 mM $MgSO4$, 137 mM NaCl, 0.336 mM $Na2HPO4$, 4.166 mM $NaHCO3$, and 5.55 mM d-glucose. Cells were then incubated with HBSS containing 200 μM L-glutamic acid (G-1251, Sigma-Aldrich, Overijse, BE) during 4 h. Culture supernatant was collected, and glutamate concentration in the medium was measured using a glutamate colorimetric

assay kit according to the manufacturer's instructions (#MAK004, Sigma-Aldrich, Overijse, BE). Total extracellular glutamate reflects the sum of glutamate uptake and release activities.

4.7. Statistics

Unless specified, all results were expressed as mean values ± Standard Error of Mean (SEM). Mann–Whitney was used to assess statistical significance between two groups. For multiple comparisons (≥ 3 groups), one-way non-parametric ANOVA test followed by Kruskal-Wallis *post-hoc* analysis was used to compare each MOI condition. When groups had to be compared based on two parameters (e.g. cell type and MOI), two-way non-parametric ANOVA test followed by Dunnett's post-hoc analysis was used. The level of significance was set at $p < 0.05$. The statistical analyses were performed using the software GraphPad Prism version 7 (GraphPad Software, La Jolla, USA).

Author contribution

Data curation, Formal analysis, Methodology: V.B., K.W., N.A., K.D, R.L., N.N.
Conceptualization, Writing – Original Draft Preparation: N.G., C.N. Writing – Review & Editing: J.G., N.G.

Conflicts of interest

The authors declare no conflict of interest.

Submission declaration

This manuscript has not been published or is being reviewed elsewhere.

Appendix A. Supplementary data

Supplementary data to this article can be found online at https://doi. org/10.1016/j.brainres.2021.147344.

References

Asadi-Pooya, A.A., Simani, L., 2020. Central nervous system manifestations of COVID-19: a systematic review. J. Neurol. Sci. 413, 116832.

Bulfamante, G., Chiumello, D., Canevini, M.P., Priori, A., Mazzanti, M., Centanni, S., Felisati, G., 2020. First ultrastructural autoptic findings of SARS -Cov-2 in olfactory pathways and brainstem. Minerva Anestesiol. 86, 678–679.

Bullen, C.K., Hogberg, H.T., Bahadirli-Talbott, A., Bishai, W.R., Hartung, T., Keuthan, C., Looney, M.M., Pekosz, A., Romero, J.C., Sillé, F.C.M., Um, P., Smirnova, L., 2020. Infectability of human BrainSphere neurons suggests neurotropism of SARS-CoV-2. Altex 37, 665–671.

Cantuti-Castelvetri, L., Ojha, R., Pedro, L.D., Djannatian, M., Franz, J., Kuivanen, S., van der Meer, F., Kallio, K., Kaya, T., Anastasina, M., Smura, T., Levanov, L., Szirovicza, L., Tobi, A., Kallio-Kokko, H., Österlund, P., Joensuu, M., Meunier, F.A., Butcher, S.J., Winkler, M.S., Mollenhauer, B., Helenius, A., Gokce, O., Teesalu, T., Hepojoki, J., Vapalahti, O., Stadelmann, C., Balistreri, G., Simons, M., 2020. Neuropilin-1 facilitates SARS-CoV-2 cell entry and infectivity. Science 370, 856–860.

Chen, N., Zhou, M., Dong, X., Qu, J., Gong, F., Han, Y., Qiu, Y., Wang, J., Liu, Y., Wei, Y., Xia, J., Yu, T., Zhang, X., Zhang, L., 2020. Epidemiological and clinical characteristics of 99 cases of 2019 novel coronavirus pneumonia in Wuhan, China: a descriptive study. Lancet 395, 507–513.

Chu, H., Chan, J.F., Yuen, T.T., Shuai, H., Yuan, S., Wang, Y., Hu, B., Yip, C.C., Tsang, J. O., Huang, X., Chai, Y., Yang, D., Hou, Y., Chik, K.K., Zhang, X., Fung, A.Y., Tsoi, H. W., Cai, J.P., Chan, W.M., Ip, J.D., Chu, A.W., Zhou, J., Lung, D.C., Kok, K.H., To, K. K., Tsang, O.T., Chan, K.H., Yuen, K.Y., 2020. Comparative tropism, replication kinetics, and cell damage profiling of SARS-CoV-2 and SARS-CoV with implications for clinical manifestations, transmissibility, and laboratory studies of COVID-19: an observational study. Lancet Microbe. 1, e14–e23.

Coolen, T., Lolli, V., Sadeghi, N., Rovai, A., Trotta, N., Taccone, F.S., Creteur, J., Henrard, S., Goffard, J.C., De Witte, O., Naeije, G., Goldman, S., De Tiege, X., 2020. Early postmortem brain MRI findings in COVID-19 non-survivors. Neurology.

Coupeau, D., Burton, N., Lejeune, N., Loret, S., Petit, A., Pejakovic, S., Poulain, F., Bonil, L., Trozzi, G., Wiggers, L., Willemart, K., André, E., Laenen, L., Cuypers, L., Van Ranst, M., Bogaerts, P., Muylkens, B., Gillet, N.A., 2020. SARS-CoV-2 detection for diagnosis purposes in the setting of a molecular biology research lab. Methods Protoc. 3.

Gu, J., Gong, E., Zhang, B., Zheng, J., Gao, Z., Zhong, Y., Zou, W., Zhan, J., Wang, S., Xie, Z., Zhuang, H., Wu, B., Zhong, H., Shao, H., Fang, W., Gao, D., Pei, F., Li, X., He, Z., Xu, D., Shi, X., Anderson, V.M., Leong, A.S., 2005. Multiple organ infection and the pathogenesis of SARS. J. Exp. Med. 202, 415–424.

Gupta, A., Madhavan, M.V., Sehgal, K., Nair, N., Mahajan, S., Sehrawat, T.S., Bikdeli, B., Ahluwalia, N., Ausiello, J.C., Wan, E.Y., Freedberg, D.E., Kirtane, A.J., Parikh, S.A., Maurer, M.S., Nordvig, A.S., Accili, D., Bathon, J.M., Mohan, S., Bauer, K.A., Leon, M.B., Krumholz, H.M., Uriel, N., Mehra, M.R., Elkind, M.S.V., Stone, G.W., Schwartz, A., Ho, D.D., Bilezikian, J.P., Landry, D.W., 2020. Extrapulmonary manifestations of COVID-19. Nat. Med. 26, 1017–1032.

Helms, J., Kremer, S., Merdji, H., Clere-Jehl, R., Schenck, M., Kummerlen, C., Collange, O., Boulay, C., Fafi-Kremer, S., Ohana, M., Anheim, M., Meziani, F., 2020. Neurologic features in severe SARS-CoV-2 infection. N. Engl. J. Med. 382, 2268–2270.

Hoffmann, M., Kleine-Weber, H., Schroeder, S., Krüger, N., Herrler, T., Erichsen, S., Schiergens, T.S., Herrler, G., Wu, N.H., Nitsche, A., Müller, M.A., Drosten, C., Pöhlmann, S., 2020. SARS-CoV-2 cell entry depends on ACE2 and TMPRSS2 and is blocked by a clinically proven protease inhibitor. Cell 181, 271–280.e8.

Kanberg, N., Ashton, N.J., Andersson, L.M., Yilmaz, A., Lindh, M., Nilsson, S., Price, R. W., Blennow, K., Zetterberg, H., Gisslén, M., 2020. Neurochemical evidence of astrocytic and neuronal injury commonly found in COVID-19. Neurology. 95, e1754–e1759.

Kilinc, D., van de Pasch, S., Doets, A.Y., Jacobs, B.C., van Vliet, J., Garssen, M.P.J., 2020. Guillain-Barré syndrome after SARS-CoV-2 infection. Eur. J. Neurol.

Kumari, P., Rothan, H.A., Natekar, J.P., Stone, S., Pathak, H., Strate, P.G., Arora, K., Brinton, M.A., Kumar, M., 2021. Neuroinvasion and encephalitis following intranasal inoculation of SARS-CoV-2 in K18-hACE2 Mice. Viruses 13.

Lu, R., Zhao, X., Li, J., Niu, P., Yang, B., Wu, H., Wang, W., Song, H., Huang, B., Zhu, N., Bi, Y., Ma, X., Zhan, F., Wang, L., Hu, T., Zhou, H., Hu, Z., Zhou, W., Zhao, L., Chen, J., Meng, Y., Wang, J., Lin, Y., Yuan, J., Xie, Z., Ma, J., Liu, W.J., Wang, D., Xu, W., Holmes, E.C., Gao, G.F., Wu, G., Chen, W., Shi, W., Tan, W., 2020. Genomic characterisation and epidemiology of 2019 novel coronavirus: implications for virus origins and receptor binding. Lancet 395, 565–574.

Mahmoud, S., Gharagozloo, M., Simard, C., Gris, D., 2019. Astrocytes maintain glutamate homeostasis in the CNS by controlling the balance between glutamate uptake and release. Cells 8.

Mao, L., Jin, H., Wang, M., Hu, Y., Chen, S., He, Q., Chang, J., Hong, C., Zhou, Y., Wang, D., Miao, X., Li, Y., Hu, B., 2020a. Neurologic manifestations of hospitalized patients with coronavirus disease 2019 in Wuhan, China. JAMA Neurol. 77, 683–690.

Mao, L., Wang, M., Chen, S., He, Q., Chang, J., Hong, C., Zhou, Y., Wang, D., Li, Y., Jin, H., Hu, B., 2020. Neurological Manifestations of Hospitalized Patients with COVID-19 in Wuhan, China: a retrospective case series study. medRxiv. 2020.02.22.20026500.

Meinhardt, J., Radke, J., Dittmayer, C., Franz, J., Thomas, C., Mothes, R., Laue, M., Schneider, J., Brünink, S., Greuel, S., Lehmann, M., Hassan, O., Aschman, T., Schumann, E., Chua, R.L., Conrad, C., Eils, R., Stenzel, W., Windgassen, M., Rößler, L., Goebel, H.H., Gelderblom, H.R., Martin, H., Nitsche, A., Schulz-Schaeffer, W.J., Hakroush, S., Winkler, M.S., Tampe, B., Scheibe, F., Körtvélyessy, P., Reinhold, D., Siegmund, B., Kühl, A.A., Elezkurtaj, S., Horst, D., Oesterhelweg, L., Tsokos, M., Ingold-Heppner, B., Stadelmann, C., Drosten, C., Corman, V.M., Radbruch, H., Heppner, F.L., 2020. Olfactory transmucosal SARS-CoV-2 invasion as a port of central nervous system entry in individuals with COVID-19. Nat. Neurosci.

Moriguchi, T., Harii, N., Goto, J., Harada, D., Sugawara, H., Takamino, J., Ueno, M., Sakata, H., Kondo, K., Myose, N., Nakao, A., Takeda, M., Haro, H., Inoue, O., Suzuki-Inoue, K., Kubokawa, K., Ogihara, S., Sasaki, T., Kinouchi, H., Kojin, H., Ito, M.,

Onishi, H., Shimizu, T., Sasaki, Y., Enomoto, N., Ishihara, H., Furuya, S., Yamamoto, T., Shimada, S., 2020. A first case of meningitis/encephalitis associated with SARS-Coronavirus-2. Int. J. Infect. Dis. 94, 55–58.

Netland, J., Meyerholz, D.K., Moore, S., Cassell, M., Perlman, S., 2008. Severe acute respiratory syndrome coronavirus infection causes neuronal death in the absence of encephalitis in mice transgenic for human ACE2. J. Virol. 82, 7264–7275.

Ortiz, M.E., Thurman, A., Pezzulo, A.A., Leidinger, M.R., Klesney-Tait, J.A., Karp, P.H., Tan, P., Wohlford-Lenane, C., McCray Jr., P.B., Meyerholz, D.K., 2020. Heterogeneous expression of the SARS-Coronavirus-2 receptor ACE2 in the human respiratory tract. EBioMedicine 60, 102976.

Paniz-Mondolfi, A., Bryce, C., Grimes, Z., Gordon, R.E., Reidy, J., Lednicky, J., Sordillo, E.M., Fowkes, M., 2020. Central nervous system involvement by severe acute respiratory syndrome coronavirus-2 (SARS-CoV-2). J. Med. Virol. 92, 699–702.

Paterson, R.W., Brown, R.L., Benjamin, L., Nortley, R., Wiethoff, S., Bharucha, T., Jayaseelan, D.L., Kumar, G., Raftopoulos, R.E., Zambreanu, L., Vivekanandam, V., Khoo, A., Geraldes, R., Chinthapalli, K., Boyd, E., Tuzlali, H., Price, G., Christofi, G., Morrow, J., McNamara, P., McLoughlin, B., Lim, S.T., Mehta, P.R., Levee, V., Keddie, S., Yong, W., Trip, S.A., Foulkes, A.J.M., Hotton, G., Miller, T.D., Everitt, A. D., Carswell, C., Davies, N.W.S., Yoong, M., Attwell, D., Sreedharan, J., Silber, E., Schott, J.M., Chandratheva, A., Perry, R.J., Simister, R., Checkley, A., Longley, N., Farmer, S.F., Carletti, F., Houlihan, C., Thom, M., Lunn, M.P., Spillane, J., Howard, R., Vincent, A., Werring, D.J., Hoskote, C., Jäger, H.R., Manji, H., Zandi, M. S., 2020. The emerging spectrum of COVID-19 neurology: clinical, radiological and laboratory findings. Brain 143, 3104–3120.

Pemberton, K., Mersman, B., Xu, F., 2018. Using ImageJ to assess neurite outgrowth in mammalian cell cultures: research data quantification exercises in undergraduate neuroscience lab. J. Undergrad. Neurosci. Educ. 16, A186–A194.

Poyiadji, N., Shahin, G., Noujaim, D., Stone, M., Patel, S., Griffith, B., 2020. COVID-19-associated acute hemorrhagic necrotizing encephalopathy: CT and MRI features. Radiology, 201187.

Puelles, V.G., Lütgehetmann, M., Lindenmeyer, M.T., Sperhake, J.P., Wong, M.N., Allweiss, L., Chilla, S., Heinemann, A., Wanner, N., Liu, S., Braun, F., Lu, S., Pfefferle, S., Schröder, A.S., Edler, C., Gross, O., Glatzel, M., Wichmann, D., Wiech, T., Kluge, S., Pueschel, K., Aepfelbacher, M., Huber, T.B., 2020. Multiorgan and renal tropism of SARS-CoV-2. N. Engl. J. Med. 383, 590–592.

Radzikowska, U., Ding, M., Tan, G., Zhakparov, D., Peng, Y., Wawrzyniak, P., Wang, M., Li, S., Morita, H., Altunbulakli, C., Reiger, M., Neumann, A.U., Lunjani, N., Traidl-Hoffmann, C., Nadeau, K.C., O'Mahony, L., Akdis, C., Sokolowska, M., 2020. Distribution of ACE2, CD147, CD26, and other SARS-CoV-2 associated molecules in tissues and immune cells in health and in asthma, COPD, obesity, hypertension, and COVID-19 risk factors. Allergy 75, 2829–2845.

Ramani, A., Müller, L., Ostermann, P.N., Gabriel, E., Abida-Islam, P., Müller-Schiffmann, A., Mariappan, A., Goureau, O., Gruell, H., Walker, A., Andrée, M., Hauka, S., Houwaart, T., Dilthey, A., Wohlgemuth, K., Omran, H., Klein, F., Wieczorek, D., Adams, O., Timm, J., Korth, C., Schaal, H., Gopalakrishnan, J., 2020. SARS-CoV-2 targets neurons of 3D human brain organoids. EMBO J. 39, e106230.

Song, E., Zhang, C., Israelow, B., Lu-Culligan, A., Prado, A.V., Skriabine, S., Lu, P., Weizman, O.E., Liu, F., Dai, Y., Szigeti-Buck, K., Yasumoto, Y., Wang, G., Castaldi, C., Heltke, J., Ng, E., Wheeler, J., Alfajaro, M.M., Levavasseur, E., Fontes, B., Ravindra, N.G., Van Dijk, D., Mane, S., Gunel, M., Ring, A., Kazmi, S.A.J., Zhang, K., Wilen, C.B., Horvath, T.L., Plu, I., Haik, S., Thomas, J.L., Louvi, A., Farhadian, S.F., Huttner, A., Seilhean, D., Renier, N., Bilguvar, K., Iwasaki, A., 2021. Neuroinvasion of SARS-CoV-2 in human and mouse brain. J. Exp. Med. 218.

Uversky, V.N., Elrashdy, F., Aljadawi, A., Ali, S.M., Khan, R.H., Redwan, E.M., 2020. Severe acute respiratory syndrome coronavirus 2 infection reaches the human nervous system: How? J. Neurosci. Res.

Yang, L., Han, Y., Nilsson-Payant, B.E., Gupta, V., Wang, P., Duan, X., Tang, X., Zhu, J., Zhao, Z., Jaffré, F., Zhang, T., Kim, T.W., Harschnitz, O., Redmond, D., Houghton, S., Liu, C., Naji, A., Ciceri, G., Guttikonda, S., Bram, Y., Nguyen, D.T., Cioffi, M., Chandar, V., Hoagland, D.A., Huang, Y., Xiang, J., Wang, H., Lyden, D., Borczuk, A., Chen, H.J., Studer, L., Pan, F.C., Ho, D.D., tenOever, B.R., Evans, T., Schwartz, R.E., Chen, S., 2020. A human pluripotent stem cell-based platform to study SARS-CoV-2 tropism and model virus infection in human cells and organoids. Cell Stem Cell 27, 125–136.e7.

Ye, Z.C., Sontheimer, H., 1999. Glioma cells release excitotoxic concentrations of glutamate. Cancer Res. 59, 4383–4391.

Zanin, L., Saraceno, G., Panciani, P.P., Renisi, G., Signorini, L., Migliorati, K., Fontanella, M.M., 2020. SARS-CoV-2 can induce brain and spine demyelinating lesions. Acta Neurochir. (Wien) 162, 1491–1494.

Zhang, B.Z., Chu, H., Han, S., Shuai, H., Deng, J., Hu, Y.F., Gong, H.R., Lee, A.C., Zou, Z., Yau, T., Wu, W., Hung, I.F., Chan, J.F., Yuen, K.Y., Huang, J.D., 2020. SARS-CoV-2 infects human neural progenitor cells and brain organoids. Cell Res. 30, 928–931.

Zhao, K., Huang, J., Dai, D., Feng, Y., Liu, L., Nie, S., 2020. Acute myelitis after SARS-CoV-2 infection: a case report. medRxiv. 2020.03.16.20035105.